Article

Large anomalous Hall conductivity induced by spin chirality fluctuation in an ultraclean frustrated antiferromagnet PdCrO₂

Check for updates

Hoseong Jeon[1,2], Hyeongwoo Seo [1,2], Junho Seo[1,2], Yong Hyun Kim[1,2], Eun Sang Choi[3], Younjung Jo[4], Ho Nyung Lee [5], Jong Mok Ok [6] ✉ & Jun Sung Kim [1,2] ✉

Magnetic frustration, realized in the special geometrical arrangement of localized spins, often promotes topologically nontrivial spin textures in the real space and induces significantly large unconventional Hall responses. This spin Berry curvature effect in itinerant frustrated magnets mainly works with a static spin order, limiting the effective temperature range below the magnetic transition temperature and yielding the typical anomalous Hall conductivity below $\sim 10^3\,\Omega^{-1}\mathrm{cm}^{-1}$. Here we show that an ultraclean triangular-lattice antiferromagnet PdCrO₂ exhibits a large anomalous Hall conductivity up to $\sim 10^6\,\Omega^{-1}\mathrm{cm}^{-1}$ in the paramagnetic state, which is maintained far above the Neel temperature (T_N) up to $\sim 4T_N$. The reported enhancement of anomalous Hall response above T_N is attributed to the skew scattering of highly mobile Pd electrons to fluctuating but locally-correlated Cr spins with a finite spin chirality. Our findings point at an alternative route to realizing high-temperature giant anomalous Hall responses, exploiting magnetic frustration in the ultraclean regime.

The quantum nature of electrons' wavefunction manifests itself by large unconventional Hall responses when coupled to topologically nontrivial spin textures in itinerant frustrated magnets[1–6]. The resulting spin Berry curvature works as a fictitious magnetic field and induces intriguing transverse motion of charge or spin, dubbed as unconventional anomalous Hall effect (AHE) or topological Hall effect (THE). In various frustrated itinerant magnets containing triangular, Kagome, or pyrochlore lattices[1,3,6–15], this real-space Berry curvature can effectively produce a giant Hall response, offering a promising route to functionalities for spintronic applications[4,5]. However, two main limitations are faced while using magnetic frustration for realizing giant AHE. First, the magnetic frustration significantly suppresses the transition temperature of a long-range static spin order, setting the active temperature window of the large AHE at low temperatures. Second, due to the small mean free path in itinerant frustrated magnets, the corresponding Hall conductivity usually shares the limit of the anomalous Hall conductivity (AHC) $\sim e^2/h$ per atomic layer by the

momentum-space Berry curvature in ferromagnets[16,17]. These observations pose a challenge to identify new mechanisms and suitable material candidates for inducing a giant Hall response in a wide range of temperatures.

Recently, multiple spin scattering by fluctuating spin texture has been proposed to induce strong transverse motion of itinerant electrons in frustrated magnets, even above the spin ordering temperature[18–20]. This spin-cluster skew scattering is proportional to the thermal average of fluctuating spin chirality $\langle S_i \cdot (S_j \times S_k)\rangle$, where $S_{i,j,k}$ denotes localized spins at the neighboring sites i, j, and k. Thus, the corresponding AHE shares the common origin with THE due to static chiral spin orders. Experimental verification requires a model system satisfying several conditions, including strong magnetic frustration, short-range spin correlation well above the spin ordering temperature, and simple band structure without a complicated multiband effect. In this work, we show that in a triangular-lattice antiferromagnet PdCrO₂, a single Fermi surface of highly mobile electrons is responsible for a giant AHC, two orders of magnitude larger than $\sim e^2/h$ per

¹Center for Artificial Low Dimensional Electronic Systems, Institute for Basic Science (IBS), Pohang 37673, South Korea. ²Department of Physics, Pohang University of Science and Technology (POSTECH), Pohang 37673, South Korea. ³National High Magnetic Field Laboratory, Florida State University, Tallahassee, FL 32310, USA. ⁴Department of Physics, Kyungpook National University, Daegu 41566, South Korea. ⁵Materials Science and Technology Division, Oak Ridge National Laboratory, Oak Ridge, TN 37831, USA. ⁶Department of Physics, Pusan National University, Busan 46241, South Korea. ✉e-mail: okjongmok@pusan.ac.kr; js.kim@postech.ac.kr

atomic layer. The observed AHC is maintained up to ~150 K, below which short-range correlation of Cr spins exists. Our findings established a concrete example demonstrating spin chirality fluctuation as an effective source of giant anomalous Hall response at high temperatures in ultraclean frustrated antiferromagnets.

Results and discussion
Clean frustrated antiferromagnetic metal

PdCrO$_2$ is a rare example of antiferromagnetic delafossite metals, consisting of two-dimensional triangular layers of Pd and CrO$_2$ that provide highly conducting and Mott-insulating layers, respectively (Fig. 1a)[14,15,21–34]. The localized spins of Cr^{3+} cations ($S = 3/2$) are antiferromagnetically coupled with a Weiss temperature $\Theta \sim 500$ K, but magnetic frustration in the triangular lattice suppresses the long-range magnetic order with $T_N \approx 37.5$ K, yielding a high frustration factor $\Theta/T_N \sim 13$[14]. Below T_N, the resulting magnetic phase hosts a noncoplanar 120° spin structure with a $\sqrt{3} \times \sqrt{3}$ periodicity in the plane[21,28] and complex interlayer spin configuration with a possible scalar spin chirality $S_i \cdot (S_j \times S_k)$[14,23,25,26,29,30,32]. What makes PdCrO$_2$ unique is the significant Kondo-type coupling between the localized Cr spins and highly mobile Pd electrons through a characteristic O–Pd–O dumbbell structure (Fig. 1a)[24,31]. Below T_N, the highly conducting state of the Pd layers undergoes Fermi surface (FS) reconstruction of the otherwise single hexagonal FS, reflecting the Cr spin texture[15,24,25,31,33]. Above T_N, this single FS is recovered[24], while the short-range correlation Cr spins remain significant up to ~200 K[21,28]. Therefore, PdCrO$_2$ above T_N hosts a single electron band, proximity-coupled with fluctuating localized spins with magnetic frustration. These attributes endow PdCrO$_2$ with a strong candidate system for the proposed giant AHE due to spin-cluster skew scattering.

In order to accurately determine the longitudinal (ρ_{xx}) and transverse (ρ_{yx}) resistivities of highly conducting PdCrO$_2$, we employed micro-fabrication on a single crystal using the focused ion beam (FIB) technique[35]. The microfabricated crystal with a typical Hall-bar-pattern, in which an electric current flows along the [1,−1,0] axis (Fig. 1d and Supplementary Fig. S1), shows a clear kink at $T_N = 37.5$ K in the temperature-dependent $\rho_{xx}(T)$ (Fig. 1e), consistent with the bulk results[14,15]. A residual resistivity at low temperatures is $\rho_{xx} \approx 50$ nΩ cm, and the corresponding mean free path is estimated to be ~3.4 μm (or ~10^4 lattice periods), which is the highest among itinerant frustrated magnets. This highly conducting state of PdCrO$_2$ is further evidenced by strong de Haas–van Alphen (dHvA) oscillations from the torque magnetometry measurements (Fig. 1f), in good agreement with the previous reports[15,25]. These characters strongly suggest that PdCrO$_2$ is in the ultraclean regime.

Before discussing the Hall response above T_N in PdCrO$_2$, we focus on its magnetization from the localized Cr spins. The torque magnetometry offers one of the most sensitive probes on magnetic response in the paramagnetic state at high magnetic fields by detecting the torque $\tau = m \times H$, where the magnetic moment $m = \mu_0 V M$ is determined by the vacuum permeability μ_0, the sample volume V, and magnetization M. While $\tau(H)/H$ data below T_N reflects the magnetic anomaly observed at low magnetic fields[36], above T_N, one can expect an H-linear dependence $\tau/H \propto (\chi_c - \chi_a)H$, assuming a constant magnetic susceptibility ($\chi_{a,c}$) along the a or c axis, described by $M_{a,c}(H) = \chi_{a,c}H$, which differ slightly with each other even above T_N[14,21,36]. However, careful analysis revealed that τ/H curves right above T_N in PdCrO$_2$ exhibit a sizable deviation from the expected H-linear dependence. As a representative case, we plotted the τ/H data taken at 40 K together with H-linear line, described by $\tau/H \sim \alpha H$,
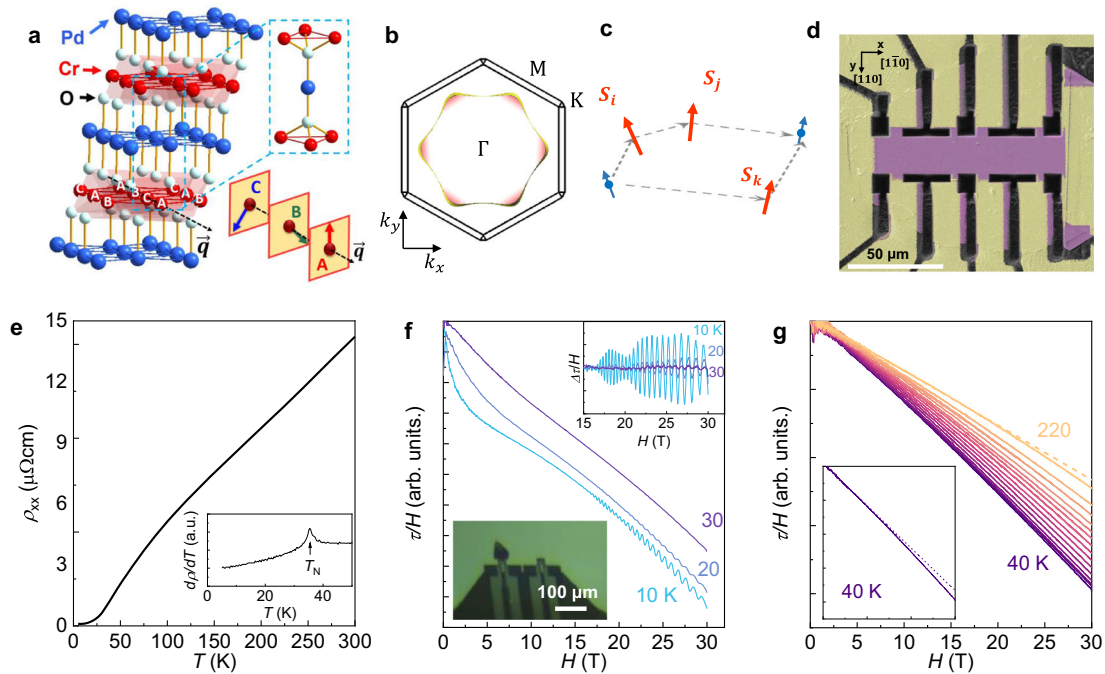

Fig. 1 | Electronic and magnetic properties of PdCrO$_2$ single crystal. a The crystal structure of PdCrO$_2$. The blue, red, and white spheres represent Pd, Cr, and O atoms, respectively. The noncollinear and noncoplanar spin structure of PdCrO$_2$ below T_N is shown along $q = (1/3, 1/3, 0)$ (yellow planes). **b** Cross section of the quasi-2D hexagonal Fermi surface (FS) above T_N. Significant quasiparticle scattering through a magnetic q-vector produces hot spots at the corners of the hexagonal FS (red-shaded areas). **c** Schematic illustration of the spin-cluster skew scattering. Asymmetric scattering arises from interference between the scattering processes (the dashed lines) with the localized spins (the red arrow) and conduction spins of electrons (the blue arrows). **d** False-color SEM images of FIB-fabricated PdCrO$_2$ single crystals carved in typical Hall bar-type patterns (purple) with gold electrodes (yellow). **e** Temperature-dependent in-plane resistivity of PdCrO$_2$ showing a clear anomaly at $T_N = 37.5$ K. **f, g** Temperature-dependent torque magnetometry signal τ/H of up to 30 T in the antiferromagnetic phase (**f**) and the paramagnetic phase (**g**). The optical image of a single crystal mounted on a piezoresistive cantilever and the observed magnetic quantum oscillations at low temperatures are shown in the insets of (**f**). Above T_N, a clear deviation from the ideal paramagnetic behavior $\tau/H \sim H$ (dashed straight line) is observed in **g** and the insets of **g**.

where the slope α is determined by the low field τ/H data below ~10 T (the inset of Fig. 1g). Here, the field range for the linear fitting is chosen to recover the unconventional linear H-dependence at the low magnetic field. The deviation $\Delta(\tau/H) = \tau/H - \alpha H$ for all measured temperatures, shown in Supplementary Fig. S2, clearly reveals the concave behavior of τ/H data, which becomes weaker with increasing temperature. This captures a signature of short-range correlation of Cr spins above T_N, unlike conventional field-linear dependence of τ/H in the paramagnetic phase.

This deviation of τ/H from the H-linear dependence, obtained under magnetic fields nearly along the c-axis, probes additional contribution (ΔM_c) to the field-linear $\sim\chi_c H$ dependence. In general, magnetization along a and c axes in the paramagnetic phase is described by $M_{a,c} = \chi_{a,c}H + \Delta M_{a,c}(H)$, where the deviation $\Delta M_{a,c}(H)$ is negligible at low magnetic fields H, but sizable at high H. For a slight tilting angle $\theta \sim 2°$, $H_a = H \sin\theta$ is much smaller than $H_c = H \cos\theta \approx H$, which means that $M_a = \chi_a H_a + \Delta M_a(H_a) \approx \chi_a H_a$, whereas $M_c = \chi_c H_c + \Delta M_c(H_c)$. Then, the resulting torque signal $\tau(H) \propto M_c H_a - M_a H_c \approx (\chi_c - \chi_a)H^2 \sin 2\theta + \Delta M_c(H)H \sin\theta$. Thus, for the τ/H data, the H-linear dependence reflects the susceptibility anisotropy, whereas its deviation from the H-linear behavior probes additional contribution to the c-axis magnetization $\Delta M_c(H)$, which can be compared with the field-dependent Hall resistivity as discussed below.

Complex magnetotransport behaviors above T_N

This short-range correlation of localized spins affects the highly mobile electrons in the paramagnetic state. The transverse resistivity $\rho_{yx}(H)$ under magnetic fields up to 17.5 T (Fig. 2a and b) exhibits complex evolution in a wide range of temperatures (5–260 K). At low temperatures, $\rho_{yx}(H)$ shows a clear concave-shaped non-linearity with magnetic fields, consistent with the

previous reports[14,15]. This concave behavior in $\rho_{yx}(H)$ is gradually suppressed with temperature, and the linear field dependence of $\rho_{yx}(H)$ is recovered at $T \sim 25$ K. The corresponding Hall coefficient $R_H = \rho_{yx}/H = -2.7 \times 10^{-4}$ cm^3/C agrees well with the expected $R_0 = 1/ne$ from the total carrier density (n) obtained by the dHvA oscillations[15,25] and angle-resolved photoemission spectroscopy (ARPES)[24,31]. Interestingly, above $T = 25$ K, the field-dependent $\rho_{yx}(H)$ curves become convex upward[15]. The convex dependence of $\rho_{yx}(H)$, maximized near T_N, becomes weaker with increasing temperature and turns into concave behavior. This complex field and temperature dependences are better displayed in the field-dependent $d\rho_{yx}(H)/dH$ at different temperatures (Fig. 2e and f). Near T_N, $d\rho_{yx}/dH$ drops well below $R_0 = 1/ne$ at low magnetic fields and then grows slowly with the magnetic field, consistent with the convex field dependence of $\rho_{yx}(H)$. Upon increasing temperature, the $d\rho_{yx}/dH$ at the low field limit rises gradually across R_0 and becomes saturated at high temperatures above ~200 K. The evolution of convex-to-concave type field dependence of $\rho_{yx}(H)$ is also clearly visible in its deviation $\Delta\rho_{yx}(H) = \rho_{yx}(H) - \alpha H$, where the slope α is determined by the low field data below ~3 T (Supplementary Fig. S2).

Considering the simple one-band FS of PdCrO$_2$ in the paramagnetic state, these complex temperature and field dependence of $\rho_{yx}(H, T)$ are highly unusual and clearly distinct from those observed in the nonmagnetic delafossite metal, PdCoO$_2$ (Supplementary Fig. S3) as recognized in the previous studies[14,15]. In PdCoO$_2$, a conventional linear-field dependent $\rho_{yx}(H) = R_0 H$ was observed at low temperatures, while a nonlinear-field dependence of $\rho_{yx}(H)$ appears in the intermediate temperatures due to the momentum (k) dependent scattering time $\tau_{tr}(k)$[37]. On the quasi-2D hexagonal FS (Fig. 1b), quasiparticle scattering occurs more strongly near the
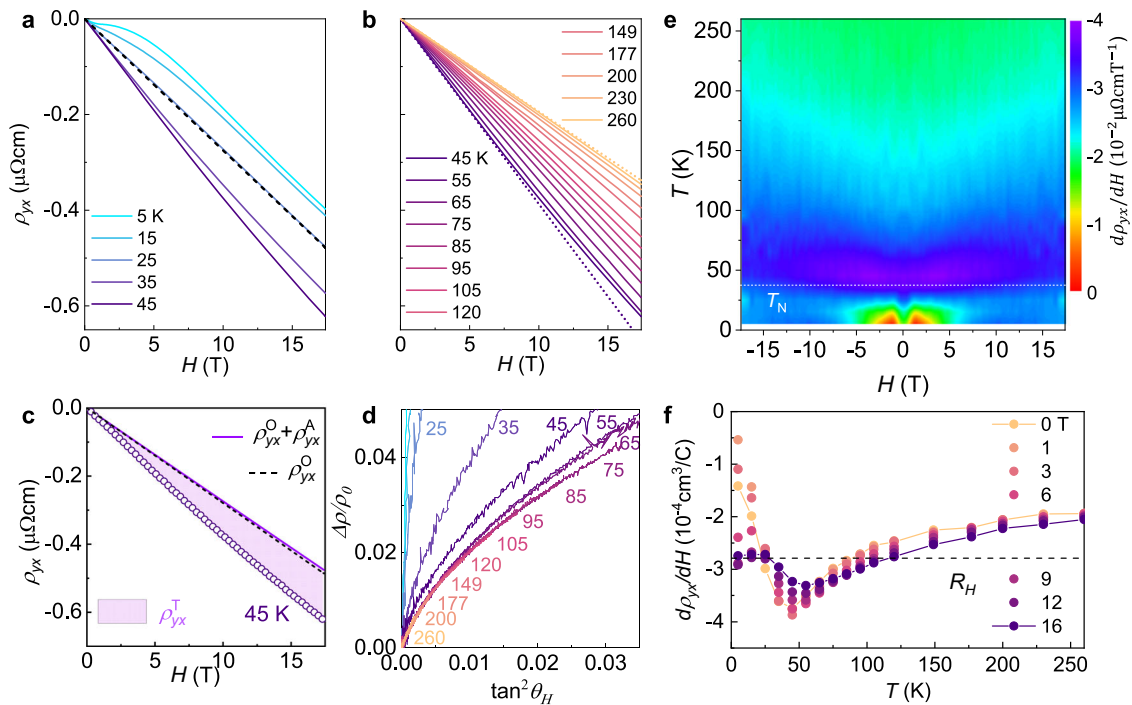

Fig. 2 | Magnetotransport properties of PdCrO$_2$ above T_N. a, b Magnetic field dependent Hall resistivity $\rho_{yx}(H)$ up to $H = 17.5$ T at different temperatures. Below T_N, $\rho_{yx}(H)$ shows a clear hump at $H \sim 5$ T (**a**), which disappears at $T \sim 25$ K, recovering the linear field dependence from a single Fermi surface (FS) (dashed line). Above T_N, $\rho_{yx}(H)$ changes from the concave to convex behaviors, manifested by opposite deviation from the low-field linear behavior (dot lines) at $T = 45$ and 260 K. **c** Deviation of $\rho_{yx}(H)$ from the conventional Hall effect (solid line), determined by the ordinary Hall ($\rho_{xy}^O(H)$) and the conventional anomalous Hall ($\rho_{yx}^A(H)$) contributions. The resulting unconventional anomalous Hall resistivity ($\rho_{yx}^T(H)$) is indicated by the shaded area. **d** The modified Kohler's plot of $\Delta\rho_{xx}(H)/\rho_{xx}(0)$ as a

function of the Hall angle, $\tan\theta_H$. Strong violation from the scaling behavior is observed below ~75 K. **e** Contour plot of $d\rho_{yx}/dH(H, T)$ at different magnetic fields and temperatures. The region of the lower $d\rho_{yx}/dH(H, T)$ is located at lower fields (violet) just above T_N, while the opposite behavior is observed with a V-shape feature at high temperatures. **f** Temperature-dependent $d\rho_{yx}/dH$ at different magnetic fields. Below $T \sim 25$ K, the high field value of $d\rho_{yx}/dH$ matches well with the calculated Hall coefficient of PdCrO$_2$, extracted from quantum oscillations. Non-monotonous temperature dependence of $d\rho_{yx}/dH$ becomes saturated at high temperatures $T \sim 150$ K.

Fig. 3 | Unconventional anomalous Hall effect above T_N. a Magnetic field-dependent unconventional anomalous Hall resistivity (ρ_{xy}^T) at different temperatures. Below $T = 25$ K, $\rho_{xy}^T(H)$ shows a positive hump, which disappears completely at $T = 25$ K. Near T_N, ρ_{xy}^T at high magnetic fields grows rapidly, followed by its suppression at high temperatures. **b** Temperature-dependent ρ_{xy}^T at $H = 17.5$ T. At $T \sim 25$ K, ρ_{xy}^T shows a sign-change from the positive (blue shaded) to the negative (red shaded) and a strong deep immediately above T_N.
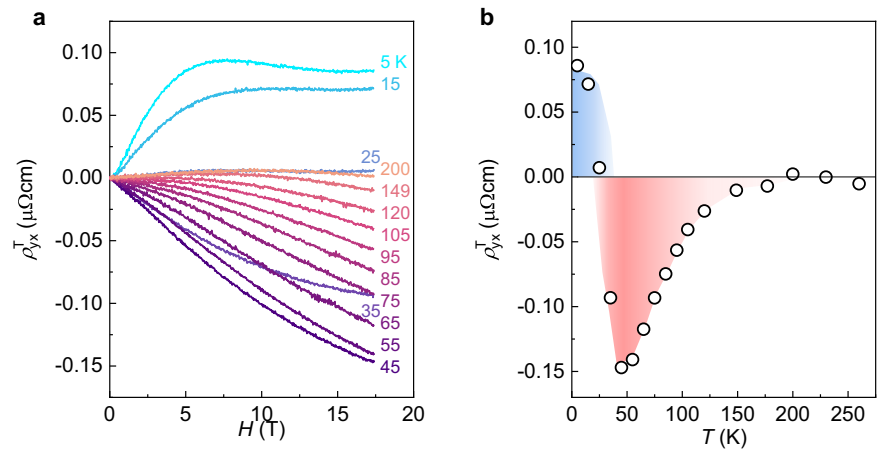
highly curved corner of the hexagonal FS, called hot spots, than near the flat part of the FS. Consequently, the Hall coefficient at low magnetic fields becomes larger than R_0 above 30 K[37,38]. In PdCrO$_2$, the fluctuating Cr spins introduce magnetic scattering with $q = (1/3, 1/3, 0)$, resulting in a significant scattering rate near the corners of the hexagonal FS[27], which has been conjectured to be responsible for unusual field-dependent Hall resistivity at high magnetic fields[15]. However, since PdCrO$_2$ shares the same hot spot structure with PdCoO$_2$ and would produce the low field dρ_{yx}/dH larger than R_0, similar to the case of PdCoO$_2$, which is opposite to what is observed experimentally in PdCrO$_2$ near T_N (Fig. 2f). Moreover, the conventional AHE, proportional to the field-dependent magnetization, cannot explain the observed behavior of $\rho_{yx}(H, T)$ in PdCrO$_2$. One of the key findings in this work is that the evolution of the concave-to-convex-type field dependence of $\rho_{yx}(H)$ with increasing temperature (Fig. 2b and Supplementary Fig. S2) is inconsistent with a monotonous convex-type field dependence of magnetization, obtained from the $\tau(H)/H$ data (Fig. 1g). These observations strongly suggest that an additional mechanism due to fluctuating spins is needed to understand the transverse motion of quasiparticles above T_N in PdCrO$_2$.

Magnetic field dependence of the longitudinal resistivity $\rho_{xx}(H)$ above T_N supports the same conclusion. In conventional metals, assuming temperature-independent anisotropy of $\tau_{tr}(k)$ on the FS, the magnetoresistance $\Delta\rho_{xx}(H)/\rho_{xx}(0)$ follows the Kohler's scaling rule $\Delta\rho_{xx}(H)/\rho_{xx}(0) = f(H/\rho_{xx}(0))$, where f denotes a temperature-independent scaling function. However, we found that Kohler's rule is strongly violated in PdCrO$_2$ for the entire temperature range up to 260 K above T_N (Supplementary Fig. S4). This behavior contrasts with the case of nonmagnetic (Pd,Pt)CoO$_2$, showing clear Kohler's scaling behaviors at $T > 150$ K[37]. Similar violation of Kohler's scaling was reported in various itinerant antiferromagnets[39–43], in which fluctuations of local spins dictate quasiparticle scattering near the hot spots. In this case, $\Delta\rho_{xx}(H)/\rho_{xx}(0)$ is scaled with the Hall angle, $\tan\theta_H = R_H H/\rho_{xx}(0)$, rather than $H/\rho_{xx}(0)$, following the modified Kohler's rule, $\Delta\rho/\rho(0) = f(\tan^2\theta_H)$. At high temperatures ($T > 75$ K), $\Delta\rho/\rho(0)$ curves of PdCrO$_2$ collapse onto a single curve, nicely following the modified Kohler's rule (Fig. 2d). However, a strong violation from the modified Kohler's rule occurs near T_N (25 K < T < 75 K), in which $\rho_{yx}(H)$ shows strong convex-shaped field dependence, which consistently suggests additional scattering channel above T_N.

Unconventional anomalous Hall effect above T_N

In order to quantify the additional unconventional AHE above T_N, we decomposed the field dependent $\rho_{yx}(H)$ into the following three terms $\rho_{yx}(H) = \rho_{xy}^O(H) + \rho_{yx}^A(H) + \rho_{yx}^T(H)$, where $\rho_{xy}^O(H) = R_0 H$ denotes the H-linear ordinary Hall contribution, reflecting a single Fermi surface in the paramagnetic state, $\rho_{yx}^A(H) \propto M(H)$ corresponds to the conventional anomalous Hall contribution proportional to finite magnetization $M(H)$

along the c axis, and $\rho_{yx}^T(H)$ represents the unconventional anomalous Hall contribution[7–13,44,44–47]. Here, we precisely determined $R_0 = 1/ne$ from both ARPES and dHvA oscillations (Fig. 1f)[15,24,31] and $M(H)$ from measurements of the magnetic susceptibilities[14,21]. For conventional anomalous Hall contribution ρ_{yx}^A, we considered two possible cases based on the dominant sources of AHE, $\rho_{yx}^A = aM\rho_{xx}^2$ for the k-space Berry curvature or the side-jump impurity scattering, or $\rho_{yx}^A = bM\rho_{xx}$ for impurity skew impurity scattering[16,17]. In both cases, a single parameter a or b was determined to reproduce the observed $\rho_{yx}(H)$ data above ~ 200 K, in which short-range spin correlation is fully suppressed in PdCrO$_2$[21,28], and assumed to be temperature independent (Supplementary Fig. S5). Then, the unconventional contribution $\rho_{yx}^T(H)$ was obtained by $\rho_{yx}^T(H) = \rho_{yx}(H) - \rho_{xy}^O(H) - \rho_{yx}^A(H)$ down to low temperatures (Fig. 3a). We note that $\rho_{yx}^T(H)$ data in the two cases mentioned above were qualitatively similar to each other (Supplementary Fig. S6). Each contribution $\rho_{yx}^O(H)$, $\rho_{yx}^A(H)$ and $\rho_{yx}^T(H)$ are plotted in Fig. 2c for $T = 45$ K as a representative case and in Supplementary Fig. S7 for all measured temperatures. We found that the weak convex behaviors of $\rho_{yx}(H)$ at high temperatures above ~150 K are well explained by the contributions of $\rho_{yx}^O(H)$ and $\rho_{yx}^A(H)$ only, while the concave behaviors of $\rho_{yx}(H)$, developed approaching to ~T_N, are due to significant contribution of $\rho_{yx}^T(H)$. We note that the conventional AHE contribution ρ_{yx}^A becomes negligible near T_N due to the rapid decrease of ρ_{xx} (Supplementary Fig. S5). Although caution needs to be taken when estimating the magnitude of $\rho_{yx}^T(H)$ below T_N, such qualitative changes suggest that the field- and temperature-dependent $\rho_{yx}^T(H, T)$ capture of the intrinsic transport properties due to fluctuating spins in PdCrO$_2$.

Magnetic field dependent $\rho_{yx}^T(H)$ above T_N is highly distinct from $\rho_{yx}^T(H)$ below T_N. While the precise magnetic structure of PdCrO$_2$ below T_N has remained controversial, a finite scalar spin chirality and the resulting THE well below T_N was proposed by H. Takatsu et al. to explain to the nonlinear field dependence of $\rho_{yx}^T(H)$[14]. This has been supported by several subsequent studies, including single crystal neutron diffraction and non-reciprocal magnetotransport measurements[23,29,30,32], although detailed field dependence of $\rho_{yx}^T(H)$ such as plateau behaviors above ~ 10 T (Fig. 3a) remains to be understood. As the static magnetic order melts down near T_N, we found that additional Hall contribution, opposite in sign, becomes developed and eventually dominant above T_N (Fig. 3b). Upon further increasing temperature, ρ_{yx}^T at $H = 17.5$ T, maximized near T_N, is gradually decayed but remains finite up to ~ 150 K (~4 T_N). This sign reversal and enhancement of ρ_{yx}^T near T_N are consistent with the theoretical predictions from the spin-cluster skew scattering model[18–20]. In frustrated magnets, a finite scalar spin chirality induces the THE[1,4] and the resulting Hall conductivity σ_{yx}^{THE} are determined by $\langle S_i \rangle \cdot \langle S_j \rangle \times \langle S_k \rangle$, where $\langle \rangle$ denotes thermal average. Thus σ_{yx}^{THE} is reduced to zero as temperature approaches to T_N. However, near T_N, fluctuating but short-range-correlated spins with a scalar spin chirality can produce asymmetric scattering due to interference

Fig. 4 | Anomalous Hall conductivities for various itinerant magnets. a Anomalous Hall ($\sigma_{xy}^{A\ or\ T}$) and longitudinal (σ_{xx}) conductivities for various ferromagnets (open symbols)[16,17] and frustrated magnets (solid symbols)[4,7–13,45–48,54–56]. For conventional ferromagnets, scaling behaviors of $\sigma_{xy}^A \sim \sigma_{xx}^\alpha$ were observed in the hopping regime (α = 1.6, green dashed line) and in the ultraclean regime (α = 1, orange dashed line), except in the intermediate regime showing a nearly constant σ_{xy}^A due to the momentum-space Berry curvature effect. For frustrated magnets, the topological Hall effect follows the trend $\sigma_{xy}^T \sim \sigma_{xx}^2$ (red dashed line). **b** The detailed scaling behavior of the candidate magnets showing a spin cluster skew scattering effect, including PdCrO$_2$ (red circles), MnGe film (navy circles), and KV$_3$Sb$_5$ (green circles). For comparison, $\sigma_{xy}^T \sim \sigma_{xx}^\alpha$ with different exponents, α is shown with the quantum conductivity e^2/ha, where a corresponds to the lattice parameter (solid cyan line). **c,** the anomalous Hall conductivity σ_{xy}^T for frustrated magnets as a function of the normalized temperature with the magnetic transition temperatures (T_c or T_N).
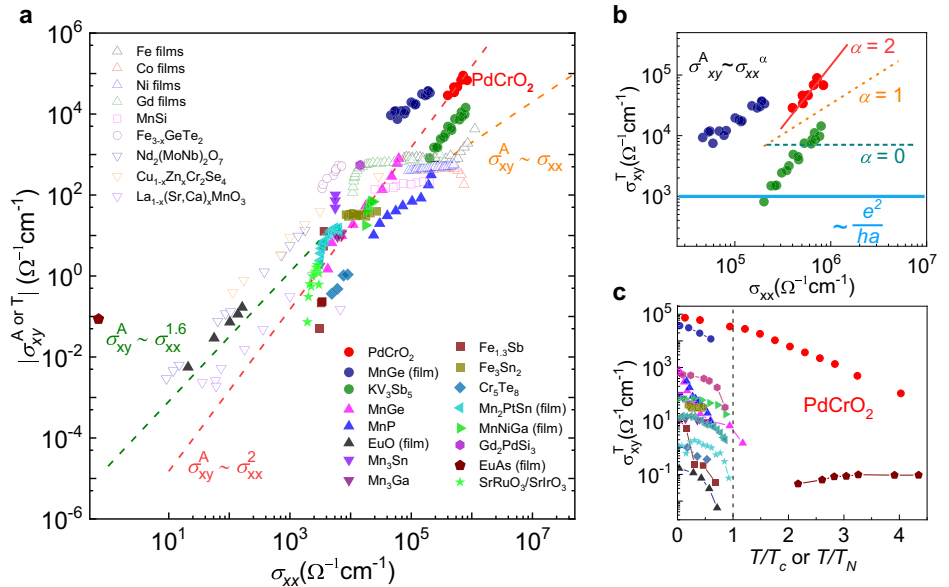
between the one- and two-spin scattering processes (Fig. 1c), named as spin-cluster skew scattering. Boltzmann calculations reveal that the resulting Hall conductivity is proportional to $\sigma_{yx}^{sk} \sim J^3 \langle S_i \cdot S_j \times S_k \rangle$, where J is Kondo coupling between itinerant electrons and localized spins[18,19]. Therefore, it can persist at high temperatures until the short-range spin correlation is fully suppressed. Moreover, for ferromagnetic Kondo coupling ($J < 0$), σ_{yx}^{THE} is opposite in sign and comparable in size with σ_{yx}^{sk}. All of such hallmarks of spin-cluster skew scattering are well reproduced in $\rho_{yx}^T(T)$ of PdCrO$_2$ (Fig. 3b). Furthermore, the resulting $\rho_{yx}^T(H)$ exhibits a characteristic non-monotonic field dependence (Fig. 3a), resembling the typical topological Hall resistivity $\rho_{xy}^T(H)$ from a static scalar spin chirality, as discussed in Supplementary Fig. S8[48].

In the spin cluster skew scattering model, the sign crossover temperature is determined by competition between σ_{yx}^{THE} and σ_{yx}^{sk}. Well below T_N, σ_{yx}^{THE} is dominant due to a static spin chiral order, but upon increasing temperature towards T_N, σ_{yx}^{sk} with an opposite sign becomes significant and eventually dominates over σ_{yx}^{THE}, leading to sign crossover of the resulting Hall conductivity. Therefore the sign crossover is expected to occur below T_N, before σ_{yx}^{THE} becomes zero at T_N, in PdCrO$_2$ at ~25 K (Fig. 3a). In fact, a specific heat study on PdCrO$_2$ found a small hump observed at ~ 20 K, due to significant fluctuations of frustrated spins[21]. The onset of spin fluctuation well below T_N in PdCrO$_2$ can suppress static spin chirality for σ_{yx}^{THE} and enhance skew scattering contribution σ_{yx}^{sk}, leading to the observed sign crossover in the Hall conductivity at ~25 K. The observed sign reversal, active temperature window, and magnetic field dependence of $\rho_{yx}^T(H, T)$ are in good agreement with the theory, suggesting that the spin-cluster skew scattering is the primary origin of $\rho_{yx}^T(H, T)$ above T_N in PdCrO$_2$.

The scaling properties of additional Hall conductivity $\sigma_{xy}^T = \rho_{yx}^T/(\rho_{xx}^2 + \rho_{yx}^2)$ with the longitudinal conductivity $\sigma_{xx} = \rho_{xx}/(\rho_{xx}^2 + \rho_{yx}^2)$ further support the spin-cluster skew scattering model in PdCrO$_2$. From the data obtained from the seven different PdCrO$_2$ crystals, we found that σ_{xy}^T is strongly enhanced with increasing σ_{xx} (Fig. 4b). Consistently, in the PdCrO$_2$ thin films[49], of which σ_{xx} is reduced by order of magnitude than single crystals, the Hall resistivity $\rho_{yx}(H)$ recovers the completely linear H dependence up to 30 T without any detectable contribution of ρ_{yx}^T (Supplementary Fig. S9). The scaling behavior of $\sigma_{xy}^T \sim \sigma_{xx}^2$, observed in PdCrO$_2$ single crystals, differs clearly from the scaling behaviors expected for the impurity skew scattering, $\sigma_{xy}^A \propto \sigma_{xx}$, or for the side jump scattering or the intrinsic k-space Berry curvature, $\sigma_{xy}^A \propto const$[16,17]. The THE with static scalar chirality and the AHE in the strong dirty limit are known to produce the same scaling relationship of $\sigma_{xy}^{A\ or\ T} \sim \sigma_{xx}^2$, but they cannot be

applied to the case of PdCrO$_2$. For the THE, it requires a long-range spin ordering, which cannot explain the significant σ_{xy}^T observed in the paramagnetic state. The strong dirty limit behavior, often found in the ferromagnetic thin films[50–52] with $\sigma_{xx} \sim 10^2$–10^4 S cm^{-1}, is also unlikely to explain our findings on PdCrO$_2$, well inside the clean regime with several orders of magnitude higher $\sigma_{xx} \sim 10^5$-10^6 Ω^{-1} cm^{-1}. Instead, the spin-cluster skew scattering model predicts the scaling, $\sigma_{xy}^T \propto \sigma_{xx}^2$, when dominant impurity scattering introduces variation in the scattering time while the scalar spin chirality $\langle S_i \cdot (S_j \times S_k) \rangle$ remains nearly intact[18]. This is indeed the case of our PdCrO$_2$ crystals with identical T_N but different impurity concentrations, where the scattering time and σ_{xx} change without spoiling the magnetism. The clear $\sigma_{xy}^T \propto \sigma_{xx}^2$ behavior in PdCrO$_2$, consistent with the theory, contrasts with the recent case of chiral magnet films of MnGe, in which both scattering time and magnetic anisotropy are tuned by thickness reduction, introducing the scaling of $\sigma_{xy}^T \sim \sigma_{xx}$[53].

Comparison with other itinerant magnets

In comparison with other itinerant magnets, including both ferromagnets and frustrated magnets, PdCrO$_2$ shows one of the highest values of $\sigma_{xx} \sim 10^6 \Omega^{-1}$ cm^{-1}, placing PdCrO$_2$ in the ultraclean regime (Fig. 4a). In the ultraclean regime, the extrinsic impurity scattering mechanism is responsible for large AHC in ferromagnets, surpassing an upper limit of $\sigma_{xy}^A = e^2/ha \sim 10^3 \Omega^{-1}$cm^{-1} ($a$ is a lattice parameter) from the intrinsic Berry curvature effect[16,17]. However, σ_{xy}^T of PdCrO$_2$ is nearly two orders of magnitude higher than the AHC by the impurity skew scattering (Fig. 4a), indicating that magnetic fluctuations with scalar spin chirality can induce skew scattering much more effectively than backward scattering in the ultraclean regime[19]. Moreover, this is also much larger than the AHC induced by the THE from static chiral spin textures found in frustrated magnets (Fig. 4a). For the THE, the scalar spin chirality or skyrmion density works as an effective fictitious magnetic field B_{eff} in the real space, leading to $\sigma_{yx}^T \sim B_{eff}\sigma_{yx}^2$. However, the observed σ_{yx}^T of frustrated magnets is far smaller than ~$10^3 \Omega^{-1}$ cm^{-1}, due to their low conductivity. Therefore, highly mobile electrons with a large scattering time are essential for intensifying the spin cluster skew scattering effect in PdCrO$_2$.

Recently, the unconventional AHC, significantly larger than ~e^2/ha, was reported in a chiral magnet MnGe[53], a Kagome metal KV$_3$Sb$_5$[54] and a triangular magnetic semiconductor EuAs[55], which has been attributed to spin-cluster skew scattering. In the case of MnGe films, magnetic-field-induced melting of the static chiral spin order leads to a large σ_{yx}^T at high magnetic fields, probably due to significant skew scattering. However,

because of a relatively short mean free path, the temperature window of the large σ_{yx}^T is limited to below ~50 K, close to the spin ordering temperature[53]. Such a narrow temperature window below ~T_N has been similarly observed in other frustrated magnets (Fig. 4c). For a Kagome metal KV_3Sb_5, the absence of signature of strong localized V spin moments[56] and the presence of the charge density wave phase in the temperature regime of a large Hall response below ~50 K[57] have raised questions on the validity of spin-cluster skew scattering model, without ruling out the possibility of the conventional multiband effect. In the triangular-lattice magnetic semiconductor EuAs[55], an unconventional AHE is observed up to ~6T_N, which has been attributed to spin cluster scattering by noncoplanar Eu^{2+} spins on the triangular lattice. However, the semiconducting character of EuAs results in a small AHC in the hopping regime. In contrast to these materials, $PdCrO_2$ exhibits a large AHC far above ~e^2/ha, persisting up to ~150 K (~4T_N) (Fig. 4c). This unique feature of $PdCrO_2$ is because its itinerant electrons maintain their high mobility well above T_N, and the skew scattering with fluctuating spin chirality remains effective at relatively high temperatures.

Conclusion

Our findings clearly demonstrate that thermally excited spin clusters with scalar spin chirality can be an effective source for large anomalous Hall responses in itinerant frustrated magnets, particularly at the ultraclean limit. Unlike the conventional intrinsic mechanisms by the static chiral spin structures, the spin cluster skew scattering mechanism works in a wide temperature range well above the magnetic-ordering temperature. These properties found in $PdCrO_2$ are mainly due to the unique layered structure where the metallic layers host highly mobile electrons coupled with the spatially separated layers of frustrated local spins. Therefore, similar to magnetic delafossites[58-60], we envision that heterostructures with clean metallic layers and frustrated magnetic layers can provide a promising material platform for even larger anomalous Hall responses at high temperatures due to proximity-coupling with the underlying spin textures and their excitations.

Methods

Single crystal growths

Single crystals of $PdCrO_2$ were grown using the flux method with a mixture of polycrystalline $PdCrO_2$ and NaCl powders. The detailed procedure is described in refs. 15,22. Furthermore, single crystals of $PdCoO_2$ were grown using a metathetical reaction method using powders of $PdCl_2$ and CoO in sealed quartz tubes, following the recipe described in refs. 61,62. X-ray diffraction and energy-dispersive spectroscopy were used to verify confirming high crystallinity and stoichiometry of the crystals.

Torque magnetometry

A small single crystal, typically ~$50 \times 50 \times 10\ \mu m^3$, was used in torque measurements and mounted onto a miniature Seiko piezoresistive cantilever as described in ref. 15. Magnetic field and temperature were controlled in a 31 T bitter magnet at the National High Magnetic Field Laboratory, Tallahassee, FL, USA.

Device preparations

The well-defined geometry of the specimen is important for precise measurements of its electronic transport, especially the Hall resistivity, because metallic delafossites have a very low resistivity with a long mean free path (especially at in-plane transport) and high anisotropy in resistivities along the ab plane and c-axis (ρ_c/ρ_{ab}). We employed the focused-ion-beam technique to prepare the devices by following the procedures described in ref. 35. Single crystals, ~$100 \times 100 \times 10\ \mu m^3$ in size, were attached to a Si/SiO_2 substrate. Metal deposition of Cr(10 nm)/Au(150 nm) was performed through a shadow mask. The direction of the current path was defined with respect to the well-defined hexagonal facets of the crystals. We used the conditions of the beam current 10 and 1 nA for rough and find structuring, respectively.

Electric transport measurements

Transport measurements for $PdCrO_2$ were performed using standard a.c. technique at a measurement frequency and current of 17.77 Hz 1 mA, respectively. We used preamplifiers in Hall measurements for accurate resistivity measurements and noise reduction. The measurements for $PdCoO_2$ were performed using d.c. technique at a current of 10 mA in a physical properties measurement system. Hall measurements were performed using standard a.c. technique at a measurement frequency and current of 17.77 Hz and 5 mA, respectively. Magnetic field and temperature control in both measurements were obtained using an Oxford variable temperature insert and an 18 T superconducting magnet.

Data availability

All data supporting the findings of this study are available within the main text and the Supplementary Information file. The data that support the findings of this study are available from the corresponding authors upon reasonable request.

References

1. Taguchi, Y., Oohara, Y., Yoshizawa, H., Nagaosa, N. & Tokura, Y. Spin chirality, Berry phase, and anomalous Hall effect in a frustrated ferromagnet. *Science* **291**, 2573–2576 (2001).
2. Bruno, P., Dugaev, V. K. & Taillefumier, M. Topological Hall effect and Berry phase in magnetic nanostructures. *Phys. Rev. Lett.* **93**, 096806 (2004).
3. Machida, Y. et al. Unconventional anomalous Hall effect enhanced by a noncoplanar spin texture in the frustrated Kondo Lattice $Pr_2Ir_2O_7$. *Phys. Rev. Lett.* **98**, 057203 (2007).
4. Nagaosa, N. & Tokura, Y. Topological properties and dynamics of magnetic skyrmions. *Nat. Nanotechnol.* **8**, 899–911 (2013).
5. Fert, A., Reyren, N. & Cros, V. Magnetic skyrmions: advances in physics and potential applications. *Nat. Rev. Mater.* **2**, 17031 (2017).
6. Kurumaji, T. et al. Skyrmion lattice with a giant topological Hall effect in a frustrated triangular-lattice magnet. *Science* **365**, 914–918 (2019).
7. Wang, Y. et al. Magnetic anisotropy and topological Hall effect in the trigonal chromium tellurides Cr_5Te_8. *Phys. Rev. B* **100**, 024434 (2019).
8. Shiomi, Y., Mochizuki, M., Kaneko, Y. & Tokura, Y. Hall effect of spin-chirality origin in a triangular-Lattice helimagnet $Fe_{1.3}Sb$. *Phys. Rev. Lett.* **108**, 056601 (2012).
9. Li, H. et al. Large topological Hall effect in a geometrically frustrated kagome magnet Fe_3Sn_2. *Appl. Phys. Lett.* **114**, 192408 (2019).
10. Liu, Z. et al. Transition from anomalous hall effect to topological hall effect in hexagonal non-collinear magnet Mn_3Ga. *Sci. Rep.* **7**, 515 (2017).
11. Ding, B. et al. Large topological Hall effect in nonchiral hexagonal MnNiGa films. *Appl. Phys. Lett.* **110**, 092404 (2017).
12. Matsuno, J. et al. Interface-driven topological Hall effect in $SrRuO_3$–$SrIrO_3$ bilayer. *Sci. Adv.* **2**, e1600304 (2016).
13. Rout, P. K., Madduri, P. V. P., Manna, S. K. & Nayak, A. K. Field-induced topological Hall effect in the noncoplanar triangular antiferromagnetic geometry of Mn_3Sn. *Phys. Rev. B* **99**, 094430 (2019).
14. Takatsu, H., Yonezawa, S., Fujimoto, S. & Maeno, Y. Unconventional anomalous Hall effect in the metallic triangular-lattice magnet $PdCrO_2$. *Phys. Rev. Lett.* **105**, 137201 (2010).
15. Ok, J. M. et al. Quantum oscillations of the metallic triangular-lattice antiferromagnet $PdCrO_2$. *Phys. Rev. Lett.* **111**, 176405 (2013).
16. Nagaosa, N., Sinova, J., Onoda, S., MacDonald, A. H. & Ong, N. P. Anomalous Hall effect. *Rev. Mod. Phys.* **82**, 1539 (2010).
17. Onoda, S., Sugimoto, N. & Nagaosa, N. Quantum transport theory of anomalous electric, thermoelectric, and thermal Hall effects in ferromagnets. *Phys. Rev. B* **77**, 165103 (2008).

18. Ishizuka, H. & Nagaosa, N. Spin chirality induced skew scattering and anomalous Hall effect in chiral magnets. *Sci. Adv.* **4**, eaap9962 (2018).

19. Ishizuka, H. & Nagaosa, N. Large anomalous Hall effect and spin Hall effect by spin-cluster scattering in the strong-coupling limit. *Phys. Rev. B* **103**, 235148 (2021).

20. Kato, Y. & Ishizuka, H. Colossal enhancement of spin-chirality-related Hall effect by thermal fluctuation. *Phys. Rev. Appl.* **12**, 021001 (2019).

21. Takatsu, H., Yoshizawa, H., Yonezawa, S. & Maeno, Y. Critical behavior of the metallic triangular-lattice Heisenberg antiferromagnet $PdCrO_2$. *Phys. Rev. B* **79**, 104424 (2009).

22. Takatsu, H. & Maeno, Y. Single crystal growth of the metallic triangular-lattice antiferromagnet $PdCrO_2$. *J. Cryst. Growth* **312**, 3461–3465 (2010).

23. Takatsu, H. et al. Magnetic structure of the conductive triangular-lattice antiferromagnet $PdCrO_2$. *Phys. Rev. B* **89**, 104408 (2014).

24. Noh, H.-J. et al. Direct observation of localized spin antiferromagnetic transition in $PdCrO_2$ by angle-resolved photoemission spectroscopy. *Sci. Rep.* **4**, 3680 (2014).

25. Hicks, C. W. et al. Quantum oscillations and magnetic reconstruction in the delafossite $PdCrO_2$. *Phys. Rev. B* **92**, 014425 (2015).

26. Daou, R., Frésard, R., Hébert, S. & Maignan, A. Impact of short-range order on transport properties of the two-dimensional metal $PdCrO_2$. *Phys. Rev. B* **92**, 245115 (2015).

27. Billington, D. et al. Magnetic frustration, short-range correlations and the role of the paramagnetic Fermi surface of $PdCrO_2$. *Sci. Rep.* **5**, 12428 (2015).

28. Le, M. D. et al. Magnetic interactions in $PdCrO_2$ and their effects on its magnetic structure. *Phys. Rev. B* **98**, 024429 (2018).

29. Park, C. & Yu, J. Twisted double-layer chiral spin structures in anti-ferromagnetic delafossite $PdCrO_2$. Preprint at *arXiv* https://arxiv.org/abs/2001.06834 (2020).

30. Komleva, E. V., Irkhin, V. Y., Solovyev, I. V., Katsnelson, M. I. & Streltsov, S. V. Unconventional magnetism and electronic state in the frustrated layered system $PdCrO_2$. *Phys. Rev. B* **102**, 174438 (2020).

31. Sunko, V. et al. Probing spin correlations using angle-resolved photoemission in a coupled metallic/Mott insulator system. *Sci. Adv.* **6**, eaaz0611 (2020).

32. Akaike, M., Nii, Y., Masuda, H. & Onose, Y. Nonreciprocal electronic transport in $PdCrO_2$: implication of spatial inversion symmetry breaking. *Phys. Rev. B* **103**, 184428 (2021).

33. Sobota, J. A. et al. Electronic structure of the metallic antiferromagnet $PdCrO_2$ measured by angle-resolved photoemission spectroscopy. *Phys. Rev. B* **88**, 125109 (2013).

34. Wen, C. et al. Probing hidden Mott gap and Incommensurate charge modulation on the polar surfaces of $PdCrO_2$. *Phys. Rev. Lett.* **131**, 116501 (2023).

35. Moll, P. J. Focused ion beam microstructuring of quantum matter. *Annu. Rev. Condens. Matter Phys.* **9**, 147–162 (2018).

36. Takatsu, H., Yonezawa, S., Michioka, C., Yoshimura, K. & Maeno, Y. Anisotropy in the magnetization and resistivity of the metallic triangular-lattice magnet $PdCrO_2$. *J. Phys. Conf. Ser.* **200**, 012198 (2010).

37. Nandi, N. et al. Unconventional magneto-transport in ultrapure $PdCoO_2$ and $PtCoO_2$. *npj Quantum Mater.* **3**, 66 (2018).

38. Ong, N. P. Geometric interpretation of the weak-field Hall conductivity in two-dimensional metals with arbitrary Fermi surface. *Phys. Rev. B* **43**, 193 (1991).

39. Harris, J. M. et al. Violation of Kohler's Rule in the normal-state magnetoresistance of $YBa_2Cu_3O_{7-\delta}$ and $La_2Sr_xCuO_4$. *Phys. Rev. Lett.* **75**, 1391–1394 (1995).

40. Nakajima, Y. et al. Magnetotransport properties governed by antiferromagnetic fluctuations in the heavy-fermion superconductor $CeIrIn_5$. *Phys. Rev. B* **77**, 214504 (2008).

41. Gnida, D., Matusiak, M. & Kaczorowski, D. Anomalous magnetotransport in the heavy-fermion superconductor Ce_2PdIn_8. *Phys. Rev. B* **85**, 060508 (2012).

42. Eom, M. J., Na, S. W., Hoch, C., Kremer, R. K. & Kim, J. S. Evolution of transport properties of $BaFe_{2-x}Ru_xAs_2$ in a wide range of isovalent Ru substitution. *Phys. Rev. B* **85**, 024536 (2012).

43. Kasahara, S. et al. Evolution from non-Fermi- to Fermi-liquid transport via isovalent doping in $BaFe_2(As_{1-x}P_x)_2$ superconductors. *Phys. Rev. B* **81**, 184519 (2010).

44. Li, Y. et al. Large topological Hall effect observed in tetragonal Mn_3PtSn Heusler thin film. *Appl. Phys. Lett.* **113**, 062406 (2018).

45. Ohuchi, Y. et al. Topological Hall effect in thin films of the Heisenberg ferromagnet EuO. *Phys. Rev. B* **91**, 245115 (2015).

46. Kanazawa, N. et al. Large topological Hall effect in a short-period helimagnet MnGe. *Phys. Rev. Lett.* **106**, 156603 (2011).

47. Shiomi, Y., Iguchi, S. & Tokura, Y. Emergence of topological Hall effect from fanlike spin structure as modified by Dzyaloshinsky–Moriya interaction in MnP. *Phys. Rev. B* **86**, 180404 (2012).

48. Wang, W. et al. Spin chirality fluctuation in two-dimensional ferromagnets with perpendicular magnetic anisotropy. *Nat. Mater.* **18**, 1054–1059 (2019).

49. Ok, J. M. et al. Pulsed-laser epitaxy of metallic delafossite $PdCrO_2$ films. *APL Mater.* **8**, 051104 (2020).

50. Xiong, Y. M., Adams, P. W. & Catelani, G. Saturation of the anomalous Hall effect in critically disordered ultrathin CNi_3 films. *Phys. Rev. Lett.* **104**, 076806 (2010).

51. Lu, Y. M., Cai, J. W., Guo, Z. & Zhang, X. X. Unconventional scaling of the anomalous Hall effect accompanying electron localization correction in the dirty regime. *Phys. Rev. B* **87**, 094405 (2013).

52. Zhang, Y., Mi, W., Wang, X. & Guo, Z. Scaling of anomalous Hall effect in amorphous CoFeB films with accompanying quantum correction. *Solid State Commun.* **215–216**, 5–11 (2015).

53. Fujishiro, Y. et al. Giant anomalous Hall effect from spin-chirality scattering in a chiral magnet. *Nat. Commun.* **12**, 317 (2021).

54. Yang, S.-Y. et al. Giant, unconventional anomalous Hall effect in the metallic frustrated magnet candidate, KV_3Sb_5. *Sci. Adv.* **6**, eabb6003 (2020).

55. Uchida, M. et al. Above-ordering-temperature large anomalous Hall effect in a triangular-lattice magnetic semiconductor. *Sci. Adv.* **7**, eabl5381 (2021).

56. Kenney, E. M., Ortiz, B. R., Wang, C., Wilson, S. D. & Graf, M. J. Absence of local moments in the kagome metal KV_3Sb_5 as determined by muon spin spectroscopy. *J. Phys.: Condens. Matter* **33**, 235801 (2021).

57. Jiang, Y.-X. et al. Unconventional chiral charge order in kagome superconductor KV_3Sb_5. *Nat. Mater.* **20**, 1353–1357 (2021).

58. Doumerc, J.-P., Wichainchai, A., Ammar, A., Pouchard, M. & Hagenmuller, P. On magnetic properties of some oxides with delafossite-type structure. *Mater. Res. Bull.* **21**, 745–752 (1986).

59. Lopes, A. M. L. et al. Local distortions in multiferroic $AgCrO_2$ triangular spin lattice. *Phys. Rev. B* **84**, 014434 (2011).

60. Wawrzyńska, E. et al. Orbital degeneracy removed by charge order in triangular antiferromagnet $AgNiO_2$. *Phys. Rev. Lett.* **99**, 157204 (2007).

61. Tanaka, M., Hasegawa, M. & Takei, H. Growth and anisotropic physical properties of $PdCoO_2$ single crystals. *J. Phys. Soc. Jpn* **65**, 3973–3977 (1996).

62. Takatsu, H. et al. Roles of high-frequency optical phonons in the physical properties of the conductive delafossite $PdCoO_2$. *J. Phys. Soc. Jpn* **76**, 104701 (2007).

Acknowledgements

Author contributions

J.S.K., J.M.O. and H.J. conceived the experiments. J.M.O., H.J., J.S., Y.J. E.S.C. and J.S.K. performed the magnetotransport measurements at high magnetic fields. J.M.O., H.J. and H.S. grew high-quality single crystals. J.M.O. and H.N.L. grew high-quality thin films. J.M.O., H.J., Y.H.K. fabricated single-crystal-devices. J.M.O., H.J. and J.S.K. co-wrote the manuscript. All authors discussed the results and commented on the paper.

Competing interests

The authors declare no competing interests.

Additional information

Supplementary information The online version contains supplementary material available at https://doi.org/10.1038/s42005-024-01652-3.

Correspondence and requests for materials should be addressed to Jong Mok Ok or Jun Sung Kim.

Peer review information *Communications Physics* thanks Hiroaki Ishizuka and the other, anonymous, reviewer(s) for their contribution to the peer review of this work. A peer review file is available.

Reprints and permissions information is available at http://www.nature.com/reprints

Publisher's note Springer Nature remains neutral with regard to jurisdictional claims in published maps and institutional affiliations.